

## Transition from amorphous boron carbide to hexagonal boron carbon nitride thin films induced by nitrogen ion assistance

R. Gago, I. Jiménez, F. Agulló-Rueda, J. M Albella, Zs. Czigány, and L. Hultman

Citation: [Journal of Applied Physics](#) **92**, 5177 (2002); doi: 10.1063/1.1512317

View online: <http://dx.doi.org/10.1063/1.1512317>

View Table of Contents: <http://scitation.aip.org/content/aip/journal/jap/92/9?ver=pdfcov>

Published by the [AIP Publishing](#)

---

### Articles you may be interested in

[Structure and properties of carbon nitride thin films synthesized by nitrogen-ion-beam-assisted pulsed laser ablation](#)

J. Vac. Sci. Technol. A **20**, 1639 (2002); 10.1116/1.1496781

[Effect of temperature on carbon nitride films synthesized by ion-beam-assisted pulsed laser deposition](#)

J. Appl. Phys. **88**, 7060 (2000); 10.1063/1.1326474

[Effects of increasing nitrogen concentration on the structure of carbon nitride films deposited by ion beam assisted deposition](#)

J. Vac. Sci. Technol. A **18**, 2277 (2000); 10.1116/1.1285993

[Study of stress evolution of boron nitride films prepared by ion assisted deposition](#)

J. Vac. Sci. Technol. A **17**, 597 (1999); 10.1116/1.581624

[Growth mechanism of cubic boron nitride thin films by ion beam assist sputter deposition](#)

J. Vac. Sci. Technol. A **15**, 1041 (1997); 10.1116/1.580427

---

The image shows the cover of the journal 'AIP Applied Physics Reviews'. It features a 3D molecular model of a crystal structure in shades of blue and white. The title 'NEW Special Topic Sections' is prominently displayed in large white letters. Below this, it says 'NOW ONLINE' in yellow, followed by 'Lithium Niobate Properties and Applications: Reviews of Emerging Trends' in white. The AIP logo and 'Applied Physics Reviews' are in the bottom right corner.

**NEW Special Topic Sections**

**NOW ONLINE**  
Lithium Niobate Properties and Applications:  
Reviews of Emerging Trends

**AIP** Applied Physics  
Reviews

# Transition from amorphous boron carbide to hexagonal boron carbon nitride thin films induced by nitrogen ion assistance

R. Gago<sup>a)</sup>

*Institut für Ionenstrahlphysik und Materialforschung, Forschungszentrum Rossendorf e.V. PF-510119, 01314 Dresden, Germany*

I. Jiménez, F. Agulló-Rueda, and J. M. Albella

*Instituto de Ciencia de Materiales de Madrid (CSIC), Cantoblanco, 28049 Madrid, Spain*

Zs. Czigány<sup>b)</sup> and L. Hultman

*Thin Films Physics Division, Department of Physics, IFM, Linköping University, S-581 83 Linköping, Sweden*

(Received 21 May 2002; accepted 12 August 2002)

Boron carbon nitride films (BCN) were grown by  $B_4C$  evaporation under concurrent  $N_2$  ion beam assistance. The films were characterized by x-ray absorption near-edge spectroscopy, infrared and Raman spectroscopies, and high-resolution transmission electron microscopy. The bonding structure and film composition correlate with the momentum transfer per incoming atom during deposition. As the momentum transfer is increased, the film structure evolves from an amorphous boron carbide network towards a hexagonal ternary compound ( $h$ -BCN) with standing basal planes. The growth of  $h$ -BCN takes place for momentum transfer in the window between 80 and 250 (eV $\times$ amu)<sup>1/2</sup>. The characteristic vibrational features of the  $h$ -BCN compounds have also been studied. Finally, the solubility limit of carbon in the hexagonal BN structure, under the working conditions of this article, is found to be  $\sim 15$  at. %. © 2002 American Institute of Physics. [DOI: 10.1063/1.1512317]

## I. INTRODUCTION

Boron carbon nitride (BCN) compounds in thin-film form have attracted considerable interest as novel materials for hard coatings applications<sup>1</sup> and as semiconductor of varying gap.<sup>2</sup> The synthesis of ternary BCN materials seems possible based on the similar structure between graphite and hexagonal boron nitride ( $h$ -BN) and between diamond and cubic boron nitride ( $c$ -BN).

The preparation of BCN films has been attained with a large variety of deposition methods.<sup>3</sup> On the one hand, cubic structures ( $c$ -BCN) are normally composed of segregated C and BN cubic phases<sup>3–5</sup> or they allow only a small amount of carbon ( $\sim 5$  at. %) in the matrix.<sup>6</sup> On the other hand, hexagonal ternary phases ( $h$ -BCN) have been successfully produced by either chemical<sup>7,8</sup> and physical<sup>9,10</sup> vapor deposition methods.

The characterization of the bonding structure of BCN compounds is not straightforward and requires discerning between a true ternary phase and a mixture of segregated binary phases. Techniques that provide information about the fine structure of the  $K$ -1s shells are suitable for this study, since they are very sensitive to the local-bonding environment for each element and can identify phases in complex systems.<sup>11</sup> Recently, we have reported the identification by means of x-ray absorption near-edge spectroscopy

(XANES)<sup>12</sup> of ternary solid-solution BCN compounds with either  $c$ -BCN<sup>6</sup> and  $h$ -BCN<sup>10</sup> structure. In this article, we get a deeper insight into the formation of the  $h$ -BCN phase by a further characterization of the films by infrared (IR) and Raman spectroscopies and high-resolution transmission electron microscopy. In addition, the investigation of the characteristic features of ternary BCN films by IR and Raman can be used to identify the formation of these phases without the need of traveling to synchrotron radiation facilities.

## II. EXPERIMENT

### A. Film deposition

The films were grown in a high vacuum chamber with a base pressure of  $2 \times 10^{-7}$  mbar on  $p$ -type (100) oriented Si substrates. Prior to entering the chamber, the substrates were cleaned in ultrasonic baths with trichloroethylene, acetone, and methanol. The deposition system is equipped with a 5-kW electron-beam evaporator and a Kaufman ion gun of 3-cm beam diameter. The carbon and boron atoms were obtained by  $e$ -beam evaporation of boron carbide ( $B_4C$ ) lumps of approximately 3 mm size. The acceleration voltage for the electron beam was set at 7 kV and the electron emission current at 75 mA. The assistance was performed with 100%  $N_2$  at ion energies between 100 and 1200 eV and ion current densities up to 0.4 mA/cm<sup>2</sup>. The ions impinged on the sample at an incident angle of 45° with respect to the substrate normal. Prior to deposition, the substrate was sputtered with 300-eV  $Ar^+$  for 2 min to enhance the film adhesion to the substrate. The deposition time was 10 min and the substrate temperature during deposition was held at 150 °C.

<sup>a)</sup> Author to whom correspondence should be addressed; electronic mail: R.Gago@fz-rossendorf.de

<sup>b)</sup> Also at: Research Institute for Technical Physics and Materials Science of Hungarian Academy of Sciences H-1525 Budapest, P.O. Box 49, electronic mail: czigany@mfa.kfki.hu

## B. Film characterization

The film thickness was measured with a Dektak 3030 profiling system with a resolution of  $\sim 1$  nm. The substrates were clamped by a holder that worked as a mask, leaving the clamped areas uncoated. This configuration allows measuring the thickness in the step created between the deposited and non-deposited areas. The thickness was measured in four different points of the sample with a dispersion around 10%, which is considered as the measurement error. The thickness of all the samples is below 300 nm.

XANES measurements were performed at the beamline SACEMOR (SA72) of the SuperAco synchrotron at LURE (Orsay, France) and at the beamline 8.2 at the Stanford Synchrotron Radiation Laboratory (Palo Alto, California). The data were acquired in the total electron yield mode by recording the current drained to the ground from the sample. The intensity was normalized to the simultaneous signal from a gold-covered grid located upstream in the x-ray path to compensate photon flux variations coming from the synchrotron ring. The sample was set up in the “magic angle” geometry ( $\sim 55^\circ$  with respect to the incident beam) to eliminate the dependence of the absorption intensity on bonding orientation.

Cross-sectional transmission electron microscopy (TEM) specimens were made by gluing slices of the samples film-to-film into the windows of Ti discs followed by mechanical thinning and polishing. Finally, the discs were thinned to electron transparency by ion-beam milling<sup>13</sup> with a 10-keV  $\text{Ar}^+$  ion beam at an angle of  $4^\circ$  with respect to the milled surface. In the final period of the process, the ion energy was decreased gradually to 1.5 keV in order to minimize surface amorphization.<sup>14</sup> The high-resolution TEM (HRTEM) investigations were made in a Philips CM20 UT transmission electron microscope operated at 200 kV with 1.9 Å resolution.

Infrared (IR) spectroscopy was recorded with a double-beam Hitachi 270-50 system. The spectra were recorded in the 250–4000  $\text{cm}^{-1}$  region with an overall spectral resolution of  $\sim 6$   $\text{cm}^{-1}$ .

Micro-Raman spectra were collected with a Renishaw Ramascope 2000 microspectrometer at an excitation wavelength of 514.5 nm. The power density on the sample was about 5  $\text{GW/m}^2$ . The spectral resolution achieved with this system is 1  $\text{cm}^{-1}$  and the spectral slit width is 4  $\text{cm}^{-1}$ .

## III. RESULTS AND DISCUSSION

### A. Growth and identification of different bonding structures

Table I compiles the growth conditions for the BCN samples considered in this work. Due to the employment of ion-beam assistance, the deposition conditions can be correlated with the momentum transfer per incoming atom during deposition. This parameter can be considered as a quantification of the ion bombardment and the equations employed for its calculation can be found elsewhere.<sup>15</sup> However, the momentum transfer cannot be taken as a universal parameter<sup>16</sup> (for example, different results would be obtained for the same momentum transfer with 100% Ar ions) but as

TABLE I. Growth conditions ( $R$ =evaporation rate,  $V_i$ =ion acceleration voltage, and  $J_i$ =ion current density) for the samples studied in this work. The samples are sorted by the ion to atom arrival ratio ( $I/A$ ) and momentum transfer per incoming atom ( $M$ ) during deposition.

Sample	$R$ (Å/s)	$V_i$ (V)	$J_i$ (mA/cm <sup>2</sup> )	$I/A$	$M$ (eV $\times$ amu) <sup>1/2</sup>
A	3	0	0	0	0
B	3	240	0.04	0.17	17
C	3	900	0.05	0.21	41
D	3	900	0.10	0.42	83
E	3	840	0.18	0.75	144
F	3	900	0.25	1.03	207

a value to compare samples grown under similar ion assistance conditions with different ion energies and ion-to-atom arrival ratios.

Figure 1 displays the XANES spectra for the different samples. The spectra of reference materials with hexagonal (graphite and  $h$ -BN), cubic (diamond and  $c$ -BN), and icosahedral-based ( $B_4C$ ) structures are also displayed. Basically, the bonding structure of the films can be divided in three groups. For only evaporated films (Sample A), we obtain an amorphous boron carbide ( $B_xC$ ) compound. We have observed that this structure is formed for momentum transfer below  $\sim 15$  (eV $\times$ amu)<sup>1/2</sup>. For momentum transfer above  $\sim 80$  (eV $\times$ amu)<sup>1/2</sup>, the samples are identified as  $h$ -BCN (Samples D–F). Finally, for momentum transfer between those windows (Samples B and C), a two-phase structure situation is observed ( $B_xC+h$ -BCN).

In the case of  $h$ -BCN, the shape of the B(1s) and N(1s) adsorption edges reveals the formation of the hexagonal structure. The formation of a ternary solid-solution compound is evidenced by the appearance of new peaks in the C(1s) edge,  $C_1$  and  $C_2$ , related with  $\pi^*$  resonances. A detailed discussion of the XANES features can be found in a previous communication.<sup>10</sup> It is important to note the increase of the relative intensity of the  $\pi^*$  resonance peak at 192 eV compared to the  $\sigma^*$  edge in the B(1s) edge. To understand the different height of the  $\pi^*$  peak, we must recall its excitonic nature, with an exciton binding energy of  $\sim 1.5$  eV<sup>17</sup> and a certain spatial extent of the perturbation produced by the 1s hole. Calculations for the  $\pi^*$  excitonic resonance of the isoelectronic compound graphite indicate a minimum radius of about five bond lengths.<sup>18</sup> Accordingly, the intensity of the  $\pi^*$  peak seems related to the hexagonal domain size or the size of the fragments of basal planes. For crystalline  $h$ -BN, the height of the  $\pi^*$  exciton is 3–5 times larger than the height of the  $\sigma^*$  edge, while for amorphous or nanocrystalline  $h$ -BN the relative  $\pi^*$  intensity decreases.<sup>19</sup> Therefore, as we increase the momentum transfer in the region of  $h$ -BCN formation, we obtain larger hexagonal domains.

Figure 2 shows the HRTEM image for (a)  $B_xC$  (Sample A) and (b)  $h$ -BCN (Sample F) compounds. Basically, HRTEM confirms the amorphous character of  $B_xC$  and shows that the  $h$ -BCN structure consists of standing basal planes, i.e., perpendicular to the substrate surface. This preferential orientation of the hexagonal planes was also observed by performing XANES angular studies.<sup>10</sup> A 3–4 nm thin amor-



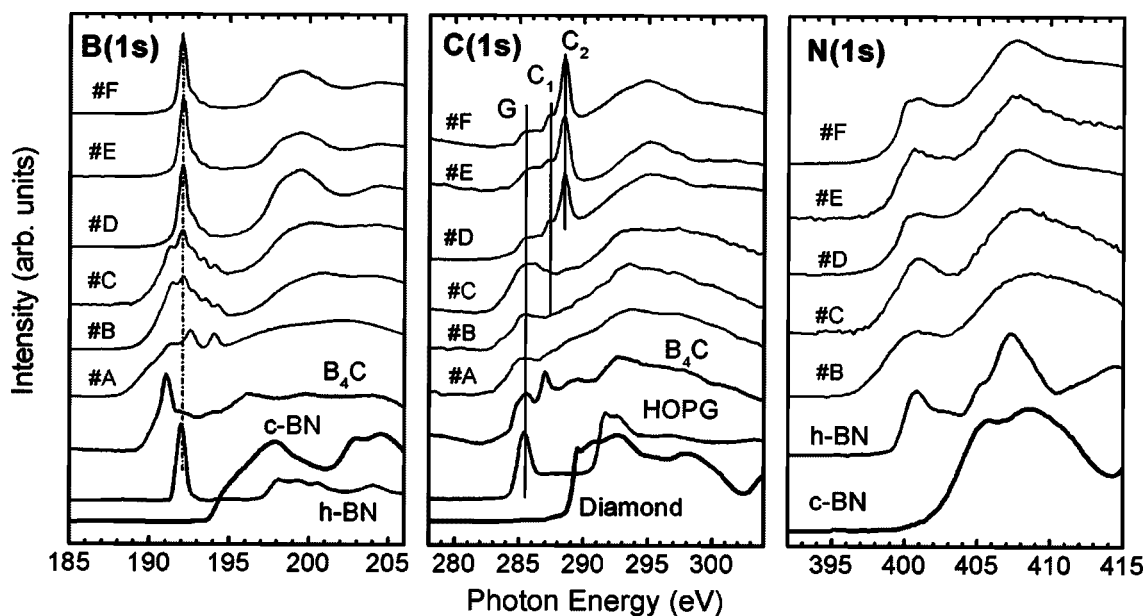


FIG. 1. XANES spectra of samples considered in this work. The spectra of reference materials with hexagonal (graphite and *h*-BN), cubic (diamond and *c*-BN), and icosahedral-based ( $B_4C$ ) structure are also displayed. The different bonding structures obtained in our films can be observed: (a)  $B_xC$  (Sample A), (b)  $B_xC + h$ -BCN (Samples B and C), and (c) *h*-BCN (Samples D-F).

phous layer between the hexagonal structure and the substrate can also be observed in Fig. 2(b). Similar layered structures have been reported for *h*-BN<sup>20</sup> and sputtered *h*-BCN.<sup>5</sup>

Figure 3 displays the composition of the films as a function of the momentum transfer. The composition of the films was determined from the XANES spectra by considering the relative intensity of the corresponding absorption edge for each element. The computation is corrected with a proportionality factor determined from comparison with BN and  $B_4C$  reference samples. The results have also been confirmed by ion-beam analysis experiments. The bonding structure (see Fig. 1) corresponding to each composition is marked in Fig. 3 with different point types. The compositional analysis

indicates that the different structures correlate mainly with the nitrogen content, which increases as the momentum transfer is higher, i.e., using a higher ion energy and/or ion to atom arrival ratio. The nitrogen uptake increases at the expense of a reduction of the boron and carbon contents, with a saturation of  $\sim 45$  at. % for momentum transfer above 150  $(\text{eV} \times \text{amu})^{1/2}$ . The amorphous  $B_xC$  structure (solid dots) is obtained for nonassisted films (no nitrogen content) and it is maintained for nitrogen contents below 15 at. %. For a nitrogen content above 30 at. %, the *h*-BCN structure (solid triangles) is promoted. Finally, for nitrogen contents between 15 and 30 at. %, a mixture of  $B_xC$  and *h*-BCN is obtained (open dots).

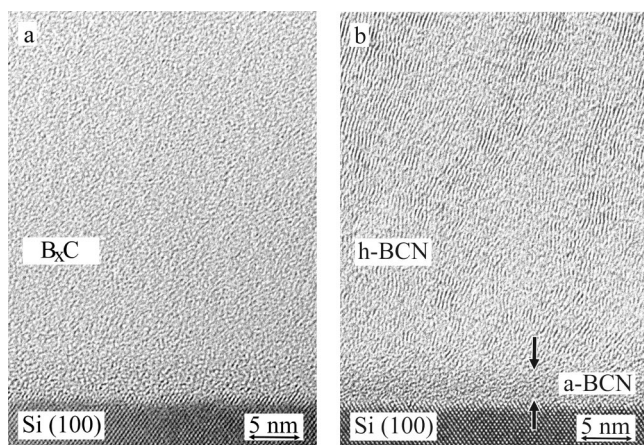


FIG. 2. HRTEM images for (a) an evaporated boron carbide film ( $B_xC$ ) and for (b) an hexagonal boron carbon nitride film (*h*-BCN). The  $B_xC$  film is amorphous while the *h*-BCN present standing basal planes. The formation of a 3–4 nm thin amorphous nucleation layer, with different contrast from the rest of the film, can be observed between the substrate and the *h*-BCN phase.

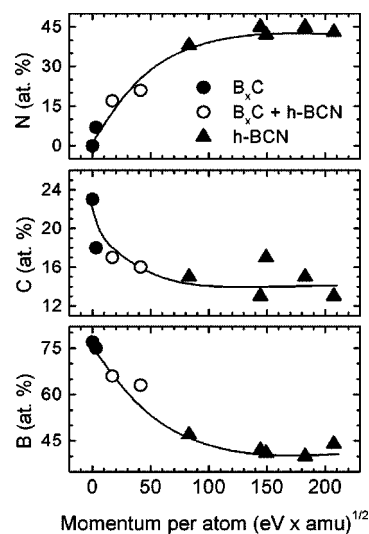


FIG. 3. Composition of the BCN films as a function of the momentum transfer during deposition. The data are derived from the relative intensity of the absorption edges in the XANES spectra. The different bonding structures are indicated with different point types.

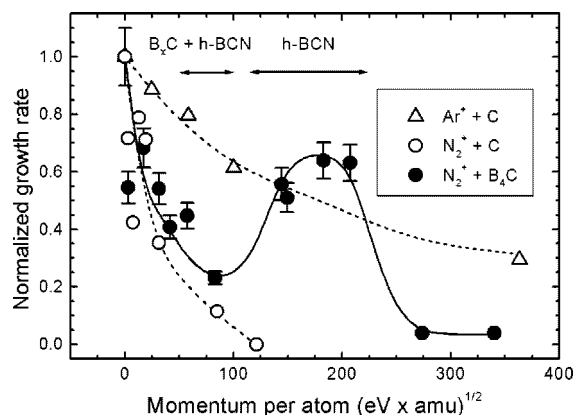


FIG. 4. Growth rate as a function of the momentum transfer during deposition for different processes:  $\text{Ar}^+$  ion bombardment during carbon evaporation ( $\Delta$ ),  $\text{N}_2^+$  ion bombardment during carbon evaporation ( $\circ$ ), and  $\text{N}_2^+$  ion bombardment during  $\text{B}_4\text{C}$  evaporation ( $\bullet$ ).

Further information about the growth process can be obtained by studying the growth rate, which is displayed in Fig. 4. In order to interpret the data we must consider that, since the evaporation rate is kept constant during the deposition, the variation on the growth rate is due to the modification of the material density, compaction or reemission of the deposited material (sputtering). The data were normalized to the growth rate obtained without ion assistance and compared with the values from argon ( $\text{Ar}^+ + \text{C}$ ) and nitrogen ( $\text{N}_2^+ + \text{C}$ ) ion bombardment during graphite evaporation. The behavior found in the case  $\text{Ar}^+ + \text{C}$  is representative of a physical sputtering process due to the inert nature of the projectile. In the  $\text{N}_2^+ + \text{C}$  experiment, note the sharp decay that is found in the growth rate with respect to the previous one. In this case, apart from the physical sputtering, we must take into account the effect of chemical sputtering coming from the formation of CN volatile species during deposition.<sup>21</sup> For  $\text{N}_2^+ + \text{B}_4\text{C}$ , we can assume that there are two competitive processes. The first process is identified as chemical sputtering, in comparison with the behavior found in the  $\text{N}_2^+ + \text{C}$  experiment. The presence of the chemical sputtering implies that the reduction of the carbon content found in our films with increasing the momentum transfer (Fig. 3) cannot be only attributed to incorporation of nitrogen in the BCN compound, but also to the loss of carbon atoms as a consequence of the formation and desorption of CN species.<sup>22</sup> The second process occurs for a narrow window between 80 and 250  $(\text{eV} \times \text{amu})^{1/2}$  and favors the film growth. In this range, the  $h\text{-BCN}$  compound is formed so these two facts may be related. Considering the density of  $\text{B}_4\text{C}$  (2.5  $\text{g}/\text{cm}^3$ ) and  $h\text{-BN}$  (2.2  $\text{g}/\text{cm}^3$ ) for a rough estimation, a change in the density could only account for a variation around  $\sim 15\%$  in the growth rate. Therefore, the sharp increase observed can only be explained by a reactive growth induced in this momentum window, which promotes the formation of the  $h\text{-BCN}$  phase. This means that the nitrogen atoms coming from the ion beam would be more efficiently incorporated to the film, reducing the sputtering process. For momentum transfer above 250  $(\text{eV} \times \text{amu})^{1/2}$  the sputtering is again the dominant process and no film growth is obtained.

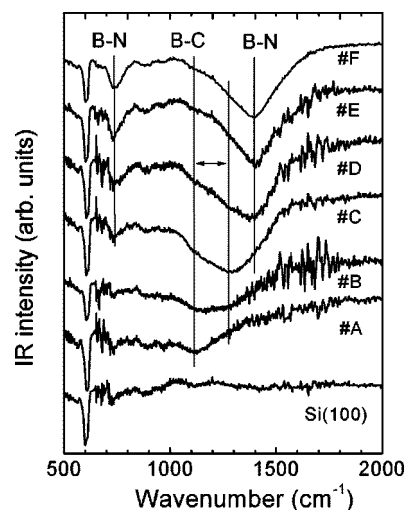


FIG. 5. IR spectra of the samples displayed in Fig. 1. The spectrum of a clean Si (100) substrate is shown for comparison purpose.

## B. Infrared (IR) spectroscopy

IR is a common characterization tool for BN compounds because is very sensitive to B–N bonds and the spectra for  $c\text{-BN}$  and  $h\text{-BN}$  show distinct features. The spectrum of  $h\text{-BN}$  is composed of two bands at 800 and 1400  $\text{cm}^{-1}$ , which arise from in-plane stretching B–N and bending B–N–B vibrations, respectively.<sup>23,24</sup> The  $c\text{-BN}$  band appears around 1050  $\text{cm}^{-1}$ ,<sup>25</sup> clearly separated from the  $h\text{-BN}$  features. The B–C vibrations in an amorphous  $\text{B}_x\text{C}$  phase appear around 1100  $\text{cm}^{-1}$  and shift to higher frequencies as the carbon content increases.<sup>26</sup> Finally, C–N modes have frequencies around 1200–1500  $\text{cm}^{-1}$ .<sup>27</sup> From the above values, it is clear that in the case of BCN films, the identification of the different phases is quite complicated due to the high number of possible combinations that appear in the same region. However, a comparison between our XANES and IR data can give useful information about the vibrational features of ternary compounds.

Figure 5 shows the IR spectra for the samples considered in Fig. 1. The spectra from a clean Si(100) substrate is also shown for comparison purposes. The sharp band at 600  $\text{cm}^{-1}$  appears in all the samples and comes from Si–Si vibrations of the substrate. The film grown without  $\text{N}_2$  ion assistance (Sample A), presents a weak band at 1100  $\text{cm}^{-1}$  related to the B–C bond in amorphous  $\text{B}_x\text{C}$ .<sup>26</sup> As the momentum transfer is increased with the  $\text{N}_2$  ion assistance, two more bands are observed. A band around 1300  $\text{cm}^{-1}$  appears for momentum transfer below 100  $(\text{eV} \times \text{amu})^{1/2}$  (Samples B and C). This band is assigned to carbon-enriched  $\text{B}_x\text{C}$ .<sup>26</sup> The formation of a carbon-enriched  $\text{B}_x\text{C}$  phase can be explained as the result of the preferential formation of B–N bonds (as we have seen, the formation of C–N bonds would lead to the development of CN volatile species), reducing the content of boron in the  $\text{B}_x\text{C}$  regions. For momentum transfer above 80  $(\text{eV} \times \text{amu})^{1/2}$  (Samples D–F), the characteristic bands of  $h\text{-BN}$  appear indicating that the hexagonal compound is formed. Equivalent features were observed in  $h\text{-BCN}$  samples grown by magnetron sputtering.<sup>22,28</sup> The similarity between the spectrum of  $h\text{-BCN}$  and  $h\text{-BN}$  may come from

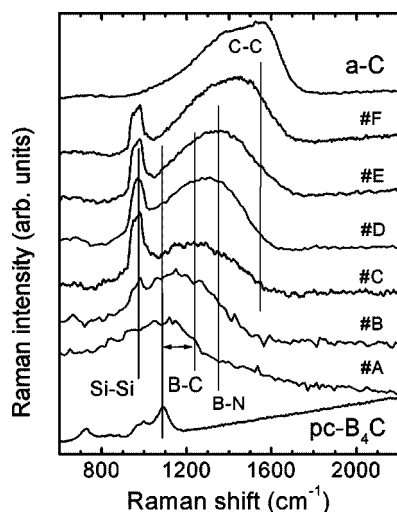


FIG. 6. Raman spectra of the samples considered in this work. The spectra of the polycrystalline boron carbide ( $pc\text{-B}_4\text{C}$ ) target and of an amorphous carbon film ( $a\text{-C}$ ) are also included.

the higher-IR sensitivity to B–N than to B–C and C–N bonds. For example, considering the intensity of the absorption peak normalized to the film thickness in the spectra of  $B_xC$  and  $h\text{-BCN}$ , we obtained a sensitivity factor five times larger in the case of B–N than in B–C bonding.

### C. Visible micro-Raman spectroscopy

Raman and IR give complementary information about the material structure due to the different selection rules for active modes. In particular, Raman is very sensitive to carbon arrangements, which are hardly detected by IR. Figure 6 shows the Raman spectra for the same samples displayed in Fig. 4. These films are highly transparent in the visible range as evidenced by the observation of Si–Si vibrations at  $960\text{ cm}^{-1}$  coming from the substrate. The spectra of the polycrystalline  $B_4C$  ( $pc\text{-B}_4C$ ) source material used for evaporation and of an amorphous carbon ( $a\text{-C}$ ) film are also displayed. The bands shown in the reference spectrum of  $pc\text{-B}_4C$  correspond to intraicosahedral modes.<sup>29,30</sup>

Basically, the same modes observed by IR are also present in the Raman spectra. However, further information is derived. The broadening of the band at  $1100\text{ cm}^{-1}$  and the disappearance of the other vibrational modes of  $pc\text{-B}_4C$ , indicate the high-amorphous character of the  $B_xC$  film (Sample A). As the transition towards the hexagonal arrangement takes place, the band position shifts toward higher frequencies. The gradual shift is an indication of the presence of different components coming from B–C, B–N, C–N, and C–C bonds. It is important to note that the Raman frequency for the hexagonal arrangement is between that of  $h\text{-BN}$  and graphite, indicating the incorporation of carbon into the hexagonal structure forming a ternary compound, as could be anticipated from XANES. In some of our  $h\text{-BCN}$  samples, we have found a Raman spectrum typical of amorphous carbon. In this case, we observed that the carbon content in these films was always above 15 at. %. This indicates that some clustering of carbon atoms may occur above this value

and, therefore, this content can be considered as a solubility limit of carbon in the hexagonal ternary structure.

### IV. CONCLUSIONS

The different BCN bonding structures obtained by  $N_2$  ion-beam assistance during the evaporation of  $B_4C$  have been identified by XANES. The resulting bonding structure and composition of the films depends on the momentum transfer during deposition. The nitrogen content increases with increasing the momentum transfer at the expense of a reduction of the boron and carbon contents, and saturates at 45 at. % for values above  $150\text{ (eV}\times\text{amu)}^{1/2}$ . The formation of C–N volatile species during deposition seems to be an additional limit to the carbon content, which decreases from 25 to 10 at. % concomitant with the nitrogen content.

For momentum transfer below  $\sim 15\text{ (eV}\times\text{amu)}^{1/2}$ , the film structure corresponds to an amorphous  $B_xC$  network, which allows nitrogen contents up to  $\sim 15$  at. %. The formation of  $h\text{-BCN}$  takes place for momentum transfer between 80 and  $250\text{ (eV}\times\text{amu)}^{1/2}$ , where nitrogen contents between 30 and 45 at. % are obtained. The hexagonal structure presents standing basal planes with a higher order as we increase the momentum transfer. Between 15 and  $80\text{ (eV}\times\text{amu)}^{1/2}$ , a phase mixture of  $B_xC$  and  $h\text{-BCN}$  is found. Above  $250\text{ (eV}\times\text{amu)}^{1/2}$ , the resputtering is dominant and no film growth is obtained.

The IR and Raman features of  $h\text{-BCN}$  have been studied. The IR spectrum resembles that of  $h\text{-BN}$  due to the higher-IR sensitivity to B–N than to B–C and C–N bonds. The Raman spectra indicate that the films are very transparent in the visible. The Raman band for  $h\text{-BCN}$  lays between that of graphite and  $h\text{-BN}$ , which indicates the incorporation of carbon into the hexagonal structure. For carbon contents above  $\sim 15$  at. % in the  $h\text{-BCN}$  films, carbon clustering takes place since the Raman spectrum is typical of amorphous carbon. This content can be considered as the solubility limit of carbon in the  $h\text{-BN}$  structure under the working conditions of this article.

### ACKNOWLEDGMENTS

This work has been partially financed under CICYT Project No. MAT99-0830 and Contract No. G5RD-CT2000-00333 from the EU as well as by the Swedish Foundation for Strategic Research (SSF) Program on Low-Temperature Thin Film Synthesis. Part of the synchrotron work was performed at the SSRL, which is supported by the U.S. Department of Energy, Office of Basic Energy Science. We are indebted to P. Parent and C. Laffon for their help with the synchrotron measurements at the LURE, which were financed by the TMR program of the EU.

<sup>1</sup>Y. Tateyama, T. Ogitsu, K. Kusakabe, and S. Tsuneyuki, Phys. Rev. B **55**, R10 161 (1997).

<sup>2</sup>A. Y. Liu, R. M. Wentzcovitch, and M. L. Cohen, Phys. Rev. B **39**, 1760 (1989).

<sup>3</sup>S. Ulrich, H. Ehrhardt, T. Theel, J. Schwan, S. Westermeyr, M. Scheib, P. Becker, H. Oechsner, G. Dollinger, and A. Bergmaier, Diamond Relat. Mater. **7**, 839 (1998).

<sup>4</sup>A. R. Badzian, Mater. Res. Bull. **16**, 1385 (1981).

<sup>5</sup>M. P. Johansson, L. Hultman, S. Daaud, K. Bewilogua, H. Lüthje, A.

- Schütze, S. Kouptsidis, and G. S. A. M. Theunissen, *Thin Solid Films* **287**, 193 (1996).
- <sup>6</sup>R. Gago, I. Jiménez, T. Sajavaara, E. Rauhala, and J. M. Albella, *Diamond Relat. Mater.* **10**, 1165 (2001).
- <sup>7</sup>M. O. Watanabe, S. Itoh, K. Mizushima, and T. Sasaki, *Appl. Phys. Lett.* **68**, 2962 (1996).
- <sup>8</sup>M. Kawaguchi, T. Kawashima, and T. Nakajima, *Chem. Mater.* **8**, 1197 (1996).
- <sup>9</sup>M. P. Johansson, H. Sjöström, and L. Hultman, *Vacuum* **53**, 451 (1999).
- <sup>10</sup>R. Gago, I. Jiménez, J. M. Albella, and L. J. Terminello, *Appl. Phys. Lett.* **78**, 3430 (2001).
- <sup>11</sup>R. Brydson, *Mater. Sci. Technol.* **16**, 1187 (2000).
- <sup>12</sup>J. Stöhr, *NEXAFS Spectroscopy* (Springer, Berlin, 1990).
- <sup>13</sup>Á. Barna, *Mater. Res. Soc. Symp. Proc.* **254**, 3 (1992).
- <sup>14</sup>Á. Barna, B. Pécz, and M. Menyhard, *Ultramicroscopy* **70**, 161 (1998).
- <sup>15</sup>D. Kester and R. Messier, *J. Appl. Phys.* **72**, 504 (1992).
- <sup>16</sup>I. Petrov, F. Adibi, J. E. Greene, L. Hultman, and J.-E. Sundgren, *Appl. Phys. Lett.* **63**, 36 (1993).
- <sup>17</sup>J. A. Carlisle, E. L. Shirley, L. J. Terminello, J. J. Jia, T. Callcott, D. L. Ederer, R. C. C. Perera, and F. J. Himpsel, *Phys. Rev. B* **59**, 7433 (1999).
- <sup>18</sup>R. Ahuja, P. A. Brühwiler, J. M. Wills, B. Johansson, N. Martensson, and O. Eriksson, *Phys. Rev. B* **54**, 14 396 (1996).
- <sup>19</sup>I. Jiménez, A. F. Jankowski, L. J. Terminello, D. G. J. Sutherland, J. A. Carlisle, G. L. Doll, W. M. Tong, D. K. Shuh, and F. J. Himpsel, *Phys. Rev. B* **55**, 12 025 (1997).
- <sup>20</sup>D. J. Kester, K. S. Ailey, R. F. Davis, and K. L. More, *J. Mater. Res.* **8**, 1213 (1993).
- <sup>21</sup>S. S. Todorov, D. Marton, K. J. Boyd, A. H. Al-Bayati, and J. W. Rabalais, *J. Vac. Sci. Technol. A* **12**, 3192 (1994); P. Hammer and W. Gissler, *Diamond Relat. Mater.* **5**, 1152 (1996); R. Kaltöfen, T. Sebal, G. Weise, *Surf. Coat. Technol.* **97**, 131 (1997).
- <sup>22</sup>M. P. Johansson, I. Ivanov, L. Hultman, E. P. Münger, and A. Schütze, *J. Vac. Sci. Technol. A* **14**, 3100 (1996).
- <sup>23</sup>R. Geik and C. H. Perry, *Phys. Rev.* **146**, 543 (1966).
- <sup>24</sup>S. P. S. Arya and A. D'Amico, *Thin Solid Films* **157**, 267 (1988).
- <sup>25</sup>P. J. Gielisse, S. S. Mitra, J. N. Plendl, R. D. Griffis, L. C. Mansur, R. Marshall, and E. A. Pascoe, *Phys. Rev.* **155**, 1039 (1967).
- <sup>26</sup>K. Shirai, S. Emura, S. Gonda, and Y. Kumashiro, *J. Appl. Phys.* **78**, 3392 (1995).
- <sup>27</sup>M. Friedrich, Th. Welzel, R. Rochotzki, H. Kupfer, and D. R. T. Zahn, *Diamond Relat. Mater.* **6**, 33 (1997).
- <sup>28</sup>A. Lousa, J. Steve, S. Muhl, and E. Martínez, *Diamond Relat. Mater.* **9**, 502 (2000).
- <sup>29</sup>D. R. Tallant, T. L. Aselage, A. N. Campbell, and D. Emin, *Phys. Rev. B* **40**, 5649 (1989).
- <sup>30</sup>T. L. Aselage, D. R. Tallant, and D. Emin, *Phys. Rev. B* **56**, 3122 (1997).